A Possible Hysteresis in the Arctic Ocean due to Release of Subsurface Heat during Sea Ice Retreat

EMMA BEER,[a] IAN EISENMAN,[a] TILL J. W. WAGNER,[b] AND ELIZABETH C. FINE[a,c]

[a] *Scripps Institution of Oceanography, University of California, San Diego, La Jolla, California*
[b] *University of Wisconsin–Madison, Madison, Wisconsin*
[c] *Woods Hole Oceanographic Institution, Woods Hole, Massachusetts*

(Manuscript received 13 June 2022, in final form 26 January 2023)

ABSTRACT: The Arctic Ocean is characterized by an ice-covered layer of cold and relatively fresh water above layers of warmer and saltier water. It is estimated that enough heat is stored in these deeper layers to melt all the Arctic sea ice many times over, but they are isolated from the surface by a stable halocline. Current vertical mixing rates across the Arctic Ocean halocline are small, due in part to sea ice reducing wind–ocean momentum transfer and damping internal waves. However, recent observational studies have argued that sea ice retreat results in enhanced mixing. This could create a positive feedback whereby increased vertical mixing due to sea ice retreat causes the previously isolated subsurface heat to melt more sea ice. Here, we use an idealized climate model to investigate the impacts of such a feedback. We find that an abrupt "tipping point" can occur under global warming, with an associated hysteresis window bounded by saddle-node bifurcations. We show that the presence and magnitude of the hysteresis are sensitive to the choice of model parameters, and the hysteresis occurs for only a limited range of parameters. During the critical transition at the bifurcation point, we find that only a small percentage of the heat stored in the deep layer is released, although this is still enough to lead to substantial sea ice melt. Furthermore, no clear relationship is apparent between this change in heat storage and the level of hysteresis when the parameters are varied.

KEYWORDS: Arctic; Feedback; Idealized models

1. Introduction

The Arctic Ocean is strongly salinity stratified, featuring a cold, relatively fresh, and often ice-covered surface layer above a halocline that has rapidly increasing salinity with depth. Below this, there is a reservoir of relatively warm, salty waters that can be a source of heat if it reaches the surface. These warmer and saltier waters have two origins. The first is Atlantic Water (AW) that flows into the Arctic Ocean through Fram Strait and the Barents Sea and resides at depths of approximately 200–800 m in much of the Arctic Ocean with temperatures around 0°–3°C (Carmack et al. 2015). The second is Pacific Water that flows into the Arctic Ocean through the Chukchi Sea and resides at depths of 50–100 m in the Canada Basin with temperatures between −1° and 1°C (Timmermans and Marshall 2020).

For much of the upper Arctic Ocean away from steep topography, vertical mixing rates are lower than in the midlatitudes (Rippeth et al. 2015). The low mixing rates have been attributed to the halocline inhibiting deep convection, low tidal energy, and sea ice damping internal waves and reducing wind momentum transfer from the atmosphere (Morison et al. 1985; Dosser and Rainville 2016). These low mixing rates prevent much of the heat stored at depth from reaching the surface (D'Asaro and Morison 1992; Fer 2009). As sea ice retreats under global warming and is replaced by open water, surface winds are expected to become more efficient at generating surface waves and internal waves (e.g., Rainville and Woodgate 2009; Liu et al. 2016), thereby leading to increased vertical mixing. This vertical mixing may increase the heat flux from the warm deep waters to the surface, which in turn will accelerate sea ice melt, thus closing a positive feedback loop. We refer to this as the "wind–ice–ocean feedback" (cf. Fine and Cole 2022). Note that similar processes have been referred to recently as the "ice/internal-wave feedback" (Dosser et al. 2021) and the "ice–ocean–heat feedback" (Polyakov et al. 2020).

This proposed feedback is supported by observations of increasing vertical heat fluxes in the Eurasian Basin coinciding with sea ice retreat and a weakening stratification during the past decade (Polyakov et al. 2017, 2020). This is related to the phenomenon widely referred to as the "Atlantification" of the Arctic Ocean (e.g., Reigstad et al. 2002; Arthun et al. 2012; Polyakov et al. 2017). The proposed feedback is further supported by observed differences in internal wave amplitudes between ice-free and ice-covered conditions. Cole et al. (2018) found that the amplitude of internal waves in the Arctic Ocean was 80% larger in ice-free regions than in completely ice-covered regions. Further, the median amplitude of internal waves in the Arctic Ocean has been found to be larger in summer than winter despite weaker winds (Dosser and Rainville 2016), suggesting that the ice cover limits the amplitude of internal waves. It has also been observed that the frequency of fall phytoplankton blooms, which have not typically been seen in the Arctic historically, are increasingly occurring (Ardyna et al. 2014). The emergence of fall blooms has been linked to increased storm activity in the fall, since strong wind events can mix nutrients up from depth (Nishino et al. 2015). On the other hand, looking at dissipation rates in the Arctic Ocean,

Corresponding author: Emma Beer, ebeer@ucsd.edu

DOI: 10.1175/JPO-D-22-0131.1

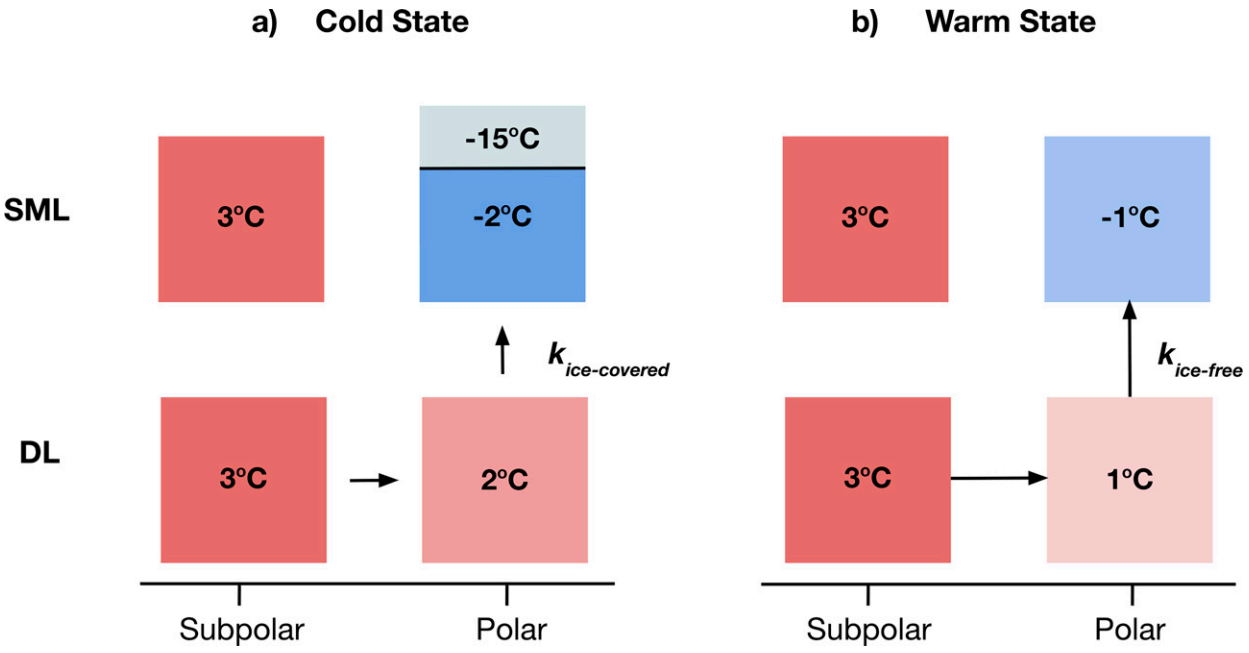

FIG. 1. Schematic of the proposed plausible bistability, showing the surface mixed layer (SML) and ocean deeper layer (DL) temperatures at subpolar latitudes and polar latitudes for (a) the cold climate state and (b) the warm climate state, which are both possible under the same climate forcing. The surface temperature of the sea ice is also shown in (a). The DL represents the Atlantic Water in polar latitudes. The vertical heat fluxes are modulated by the mixing coefficient k, which is larger under ice-free conditions than under ice-covered conditions. The length of the arrows indicates the magnitudes of the heat fluxes between boxes, which are equal to the temperature differences between the boxes multiplied by the mixing coefficients.

Rippeth et al. (2015) found no difference between ice-free and ice-covered conditions. Other measurements in the western Arctic Ocean, where upper-ocean stratification is stronger (Lincoln et al. 2016; Dosser et al. 2021; Fine et al. 2021), similarly find little evidence of elevated dissipation at depth in response to wind forcing even under ice-free conditions, indicating that this feedback may not have a large effect in the western Arctic Ocean at present.

Motivated by these observations, here we explore the dynamics of a possible wind–ice–ocean feedback in the Eurasian Basin. To investigate this feedback in isolation, we use an idealized climate model in which we specify vertical mixing rates for ice-covered and ice-free surface conditions under a range of possible parameter choices. We then investigate the possibility of hysteresis and bifurcations under climate change, as well as the changes in heat transport and storage associated with the proposed feedback.

2. A possible hysteresis

Hysteresis occurs in a system when two stable states coexist in the same parameter regime (known as a bistability) in a limited region of the parameter space, and hence the history of the system determines which state it is in. When a parameter (such as greenhouse forcing) is varied such that a system becomes no longer bistable, a bifurcation is crossed, which can lead to an abrupt transition from one state to another. This is sometimes referred to as a "tipping point." Hence, if the climate system passes such a threshold during global warming, the previous climate state cannot be recovered unless the level of greenhouse forcing is reduced substantially below its level immediately before the transition. In this case, when the greenhouse forcing is raised and then lowered, the climate system follows a hysteresis loop. Note, however, that during transient warming, the climate system is not in equilibrium and hence does not directly follow the underlying hysteresis loop, which could make bifurcation points less readily apparent.

Here we focus on the wind–ice–ocean feedback. We propose that this feedback could plausibly lead to a novel hysteresis in the climate system, implying an irreversible transition during sea ice decline. We consider a simple picture of this feedback in which vertical mixing in the upper Arctic Ocean is reduced where sea ice is present. The plausibility of multiple stable states under the same greenhouse forcing due to this feedback is illustrated schematically in Fig. 1. There is a cold climate state with polar sea ice present and hence reduced vertical mixing in the polar region, which allows the surface mixed layer to remain cold. And there is a warm ice-free state with enhanced vertical mixing which brings heat upward from the warm subsurface layer, thereby keeping the surface mixed layer warm. In the warm state, while the Arctic Ocean has a warmer surface, it actually has a colder subsurface, which is a striking signature of the proposed bistability. This is due to the enhanced upward heat flux in the polar region in the absence of sea ice, which is balanced by an enhanced horizontal heat transport in the subsurface layer. This

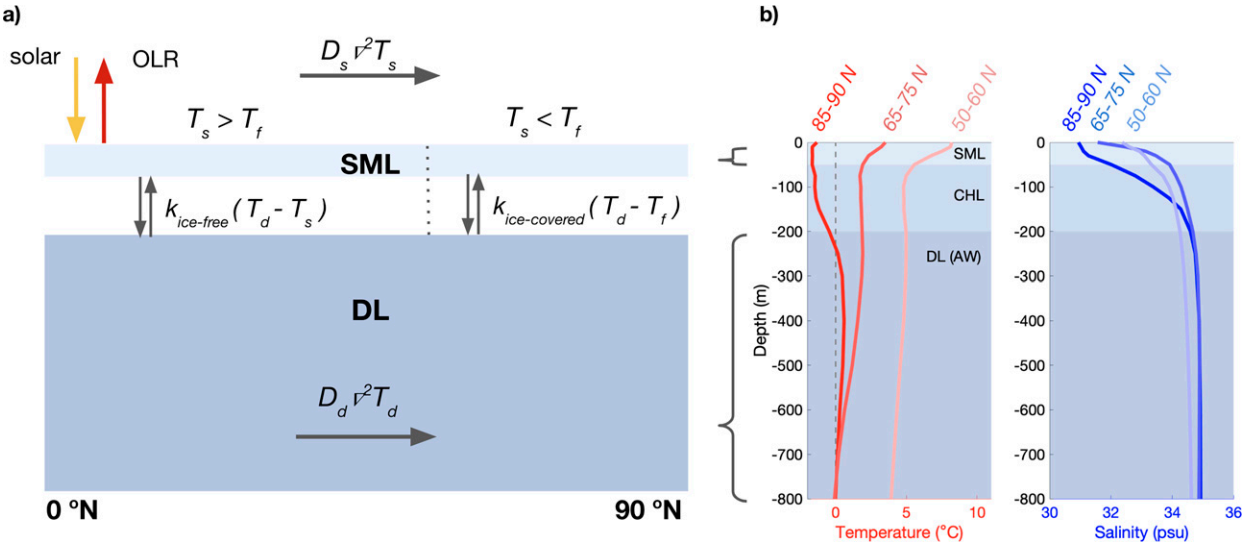

FIG. 2. (a) Schematic of the idealized climate model, which represents the latitudinally varying atmosphere, ocean surface mixed layer (SML), and ocean deeper layer (DL). In the Arctic Ocean the DL represents the Atlantic Water below the halocline. The surface temperature (T_s), DL temperature (T_d), and freezing point (T_f) are indicated, and energy fluxes represented in the model are shown as arrows. (b) Profiles of annual mean temperature and salinity from Levitus94 (Levitus et al. 1994; Levitus and Boyer 1994). Profiles are averaged zonally and over latitude ranges as labeled. The SML, cold halocline layer (CHL) where salinity rapidly increases with depth, and Atlantic Water (AW) layer are indicated. The model layers in (a) are indicative of the Arctic Ocean stratification shown by the 85°–90°N profiles in (b).

bistability can only occur for a limited range of greenhouse forcing levels. When the greenhouse forcing is so large that subfreezing Arctic surface temperatures cannot occur, there can no longer be bistability.

3. Idealized climate model

We use an idealized climate model in order to illustrate the proposed plausibility of bistable climate states supported by the wind–ice–ocean feedback. The model builds on the long-standing framework of diffusive energy balance models (EBMs). Such EBMs typically simulate the steady-state annual-mean zonal-mean surface temperature as a function of latitude within a global or hemispheric domain, based on the balance between top-of-atmosphere net solar radiation; top-of-atmosphere outgoing longwave radiation (OLR), which is approximated to depend linearly on the surface temperature; and meridional atmospheric heat transport, which is represented as diffusion of the surface temperature (Budyko 1969; Sellers 1969; North 1975).

For this study, we have added a second ocean layer to a classic EBM representation of the zonally averaged annual-mean climate in the Northern Hemisphere. The top layer is taken to represent the ocean surface mixed layer (SML) and the atmosphere above, and below this the model has an added deeper layer (DL). The DL in the Arctic Ocean represents the Atlantic Water below the halocline. This is based on the stratification in the Eurasian Basin, which is thought to be more susceptible than other regions of the Arctic to increased internal wave activity and a wind–ice–ocean feedback under warming (Davis et al. 2016; Dosser et al. 2021). Pacific Water does not constitute a well-formed layer in the Eurasian Basin, and Atlantic Water is the primary source of subsurface heat. Although the inclusion of the DL is motivated by Arctic Ocean characteristics, for simplicity we have it extend over the full hemispheric domain. Horizontal heat transport in the DL is parameterized as diffusion of the DL temperature, similar to the treatment of horizontal heat transport in the top layer. This is a crude treatment of heat transport in the ocean, which arises primarily due to large-scale advection and eddy mixing, but it offers a simple representation that moves heat from warmer regions to colder regions. The two layers are coupled using a simple representation of vertical heat flux that is proportional to the vertical temperature gradient. Hence, the model is an idealized representation of the Northern Hemisphere that focuses on changes in ocean temperature and heat transport that arise from the wind–ice–ocean feedback.

The model is illustrated schematically in Fig. 2a. The SML is chosen to be 50 m thick, as in some previous idealized models (e.g., Thorndike 1992; Eisenman and Wettlaufer 2009). Note that the observed SML depth in the Arctic Ocean varies substantially with location and season. The DL is chosen to be 600 m thick, corresponding to a depth extending from 200 to 800 m (see temperature and salinity profiles of the central Arctic in Fig. 2b). In most of the depth range of the DL, temperatures in 85°–90°N in Fig. 2b are warmer than 0°C (a typical definition of AW), and above 200 m, the salinity rapidly changes within the halocline. The halocline is not represented explicitly in the model but rather as the boundary between the two layers, so that vertical heat fluxes between the two ocean layers are interpreted as heat fluxes across the halocline. This two-layer representation is similar to the seasonally varying model used in a previous study (Beer et al. 2020), and it builds on earlier idealized two-layer column models of the climate system (e.g., Gregory 2000; Held et al. 2010).

TABLE 1. Model parameter values for the default parameter regime that approximately match observational estimates. Values for the alternative parameter regime in which hysteresis occurs are listed in parentheses and otherwise are the same as the default parameter regime values. Both regimes are shown in Fig. 4 where F is varied. In the alternative parameter regime, after D_s, D_d, and $k_{\text{ice-covered}}$ are chosen to increase the amount of hysteresis, the value of A is tuned so that the sea ice edge is at a similar latitude to the default parameter regime when $F = 0$.

Parameter	Default (alternative)	Units
c_s	6.53	W yr m^{-2} K^{-1}
c_d	78.4	W yr m^{-2} K^{-1}
α_0	0.3	
α_2	0.1	
S_0	420	W m^{-2}
S_2	240	W m^{-2}
A	192 (177)	W m^{-2}
B	2.1	W m^{-2} K^{-1}
D_s	0.5 (0.1)	W m^{-2} K^{-1}
D_d	0.15 (0.5)	W m^{-2} K^{-1}
$k_{\text{ice-free}}$	5	W m^{-2} K^{-1}
$k_{\text{ice-covered}}$	2 (1)	W m^{-2} K^{-1}
T_f	−2	°C
F	0	W m^{-2}

Note that we focus here on equilibrium model states, which do not depend on the thicknesses of the SML and DL.

As in other standard EBMs, the surface temperature T_s is determined from the balance of radiation and heat transport terms. Here we add a term representing the vertical heat flux between the SML and DL, as well as a spatially uniform climate forcing term F that can represent changes in greenhouse gases:

$$c_s \frac{\partial T_s}{\partial t} = \underbrace{(1-\alpha)S}_{\text{solar}} - \underbrace{[A + B(T_s - T_f)]}_{\text{OLR}} + \underbrace{D_s \nabla^2 T_s}_{\text{horizontal transport}} + \underbrace{k(T_d - T_{\text{SML}})}_{\text{vertical flux}} + \underbrace{F}_{\text{forcing}}, \tag{1}$$

where the net solar radiation is equal to incident solar radiation at the top of the atmosphere S minus reflected solar radiation αS with α the planetary albedo, the dependence of OLR on T_s is linearized about the freezing point T_f with constants A and B, and the constant coefficient D_s scales the equator-to-pole atmospheric heat transport.

We represent the wind–ice–ocean feedback in the model by setting the vertical heat flux between the two ocean layers to depend on the temperature difference with the coefficient

$$k = \begin{cases} k_{\text{ice-covered}}, & T_s \le T_f \\ k_{\text{ice-free}}, & T_s > T_f \end{cases}, \tag{2}$$

with $k_{\text{ice-covered}} < k_{\text{ice-free}}$. The smaller vertical heat flux coefficient under subfreezing surface temperatures represents the effects of damped internal waves and reduced momentum input from the wind when sea ice is present.

The temperature of the SML (T_{SML}) is taken to be equal to the surface temperature as long as it is above the freezing point; with colder surface temperatures, the ocean is considered to be ice-covered, and the SML below the sea ice is taken to be at the freezing point:

$$T_{\text{SML}} = \begin{cases} T_f, & T_s \le T_f \\ T_s, & T_s > T_f \end{cases}. \tag{3}$$

Hence, the top layer evolves both the surface temperature and surface mixed layer temperature, and it includes a representation of atmospheric heat transport which is a function of the surface temperature. The temperature of the DL (T_d) is determined from the balance of horizontal heat transport in the DL, which is scaled by D_d, and the vertical heat flux between the two ocean layers:

$$c_d \frac{\partial T_d}{\partial t} = \underbrace{D_d \nabla^2 T_d}_{\text{horizontal transport}} + \underbrace{k(T_{\text{SML}} - T_d)}_{\text{vertical flux}}. \tag{4}$$

The heat capacities for the SML and DL are $c_s \equiv \rho c_p H_s$ and $c_d \equiv \rho c_p H_d$, respectively, where H_s is the thickness of the SML, H_d is the thickness of the DL, ρ is the seawater density, and c_p is the seawater specific heat capacity.

To account for converging meridians on the sphere, the Laplacian operator in spherical coordinates is used for the horizontal diffusion in the SML and DL,

$$\nabla^2 = \frac{\partial}{\partial x}\left[(1-x^2)\frac{\partial}{\partial x}\right], \tag{5}$$

where $x \equiv \sin\theta$ with θ the latitude. We use as a boundary condition that there is no heat flux across the equator in either layer, which is consistent with an assumption that the annual-mean climate is hemispherically symmetric. This implies that $\partial T_{\text{SML}}/\partial x = \partial T_d/\partial x = 0$ at $x = 0$. As in previous EBM studies, we approximate the latitudinal variation in annual-mean incident solar radiation as $S = S_0 - S_2 x^2$, and we approximate the zenith angle dependence of the reflectivity of clouds by letting the planetary albedo similarly vary with latitude as $\alpha = \alpha_0 + \alpha_2 x^2$, with specified constants S_0, S_2, α_0, and α_2.

Many simplifications are made in the idealized process model in order to focus on the effects of the wind–ice–ocean feedback in isolation. However, we still expect that the inclusion of omitted features could have a substantial impact on this feedback and leave the study of these interactions to future work. For example, the model does not include seasonally varying forcing, a representation of sea ice growth and ablation, or a representation of changes in albedo associated with the onset of icy surface conditions. Here, the surface temperature is allowed to cool below the freezing point, at which point the vertical heat flux coefficient decreases, but the SML temperature remains at the freezing point. Since the surface layer is taken to be well mixed, any heat gain or loss into the layer is instantly added to the surface temperature budget [Eq. (1)]. Therefore the only thing that changes in the model equations when the surface temperature drops below the freezing point is the jump in the vertical heat flux between the two layers.

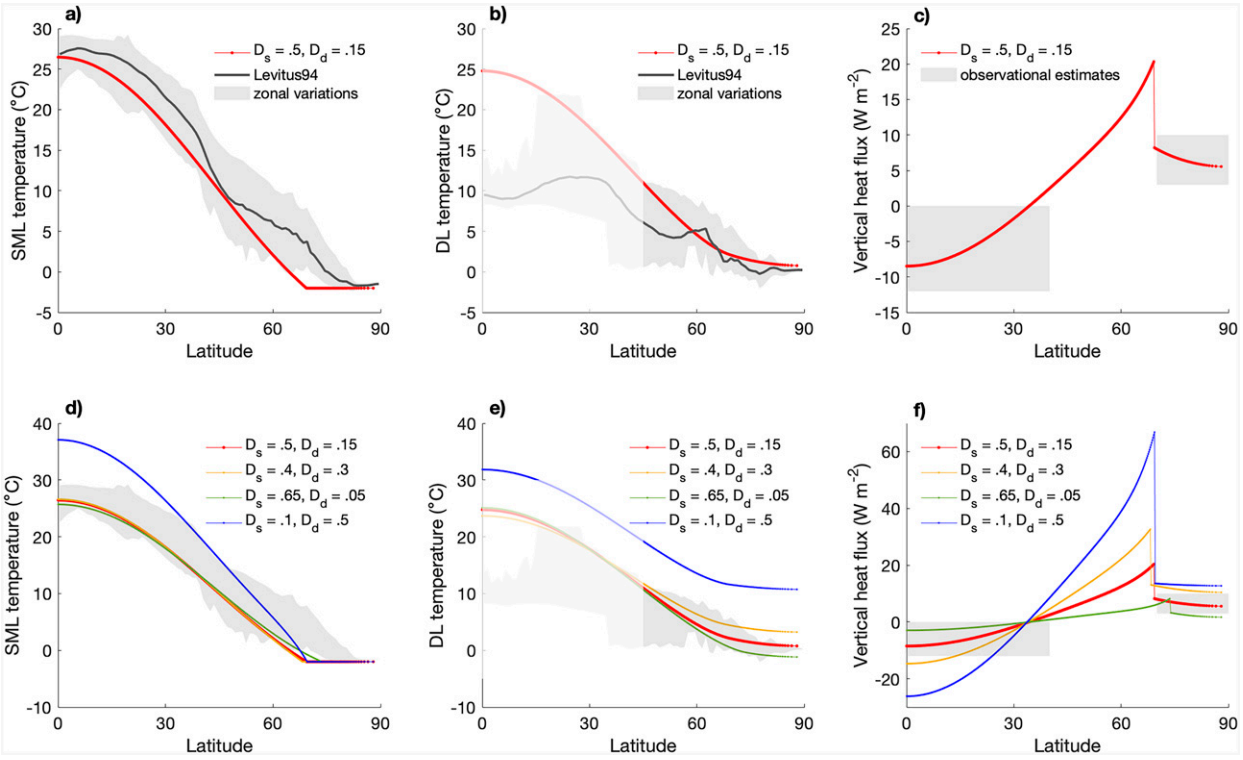

FIG. 3. (a) Surface mixed layer (SML) temperature taken as the surface temperature in ice-free conditions and the freezing point in ice-covered conditions, (b) ocean deeper layer (DL) temperature, and (c) vertical heat flux between the two layers as a function of latitude. The model results using the default parameter regime are in red. In (a) and (b), gray lines show climatology from Levitus94 (Levitus and Boyer 1994), and gray shading represents zonal variations. In (c), gray shading represents observational estimates of vertical ocean heat fluxes in the Arctic of 2–10 W m^{-2} (Carmack et al. 2015; Peterson et al. 2017; Polyakov et al. 2017), and vertical ocean heat fluxes between 0° and 40°N from −12 to 0 W m^{-2} (Cummins et al. 2016). The DL temperature south of 45°N (faded) does not match well with observations since the model does not include equatorial upwelling and other processes. (d)–(f) As in (a)–(c), with the model output for the default parameter regime in red and observational estimates in gray shading, but including the model output for the alternative parameter regime in blue and two other parameter cases with varied values of D_s and D_d. The two other parameter cases enclose the range of values of horizontal heat transport that most closely match the current climate. The values of D_s are based on values of idealized model parameters similar to D_s used in previous studies, and the values of D_d are determined by comparing the model output to observational estimates.

Two approaches are used to solve the model (1)–(5). The first approach is to numerically integrate the system in time until a steady state is reached, using implicit Euler time stepping and centered differencing in space (see appendix A for details). This allows us to simulate the time evolution of the system and provides a solution that is numerically stable for any time step size. The second approach is to use an approximate solution for the steady-state fields $T_s(x)$ and $T_d(x)$ written in terms of Legendre polynomial expansions (hereafter "steady-state solution"; see appendix B for details). This allows us to solve for both stable and unstable model states. The results presented are calculated using numerical integration unless otherwise stated.

The default parameter values are adapted from previous EBM studies and chosen to give approximate qualitative agreement with observational estimates (Table 1).

4. Idealized climate model results

Simulated fields under the default parameter regime are compared with observational estimates in Figs. 3a–c. Note, however, that given the idealized nature of the model, there is substantial uncertainty in what specific parameter values provide the best point of contact with the real world. The parameter values that give rise to the temperature field that most closely resembles observations may not give rise to the most realistic response to forced heating due to compensating errors associated with omitted physical processes. The sensitivity of the model results to changes in the horizontal transport coefficients D_s and D_d is explored in Figs. 3d–f.

a. *Bistability and hysteresis*

In the idealized climate model, the only differences between ice-free and ice-covered states are in the representations of the SML temperature and the vertical heat flux between the two ocean layers. When the surface temperature warms and crosses above the freezing point, the SML temperature is no longer fixed at T_f but freely evolves [Eq. (3)], and the vertical heat flux coefficient jumps from $k_{\text{ice-covered}}$ to $k_{\text{ice-free}}$.

We test for the possibility of bistability and hysteresis due to this nonlinear jump in vertical heat flux, as considered

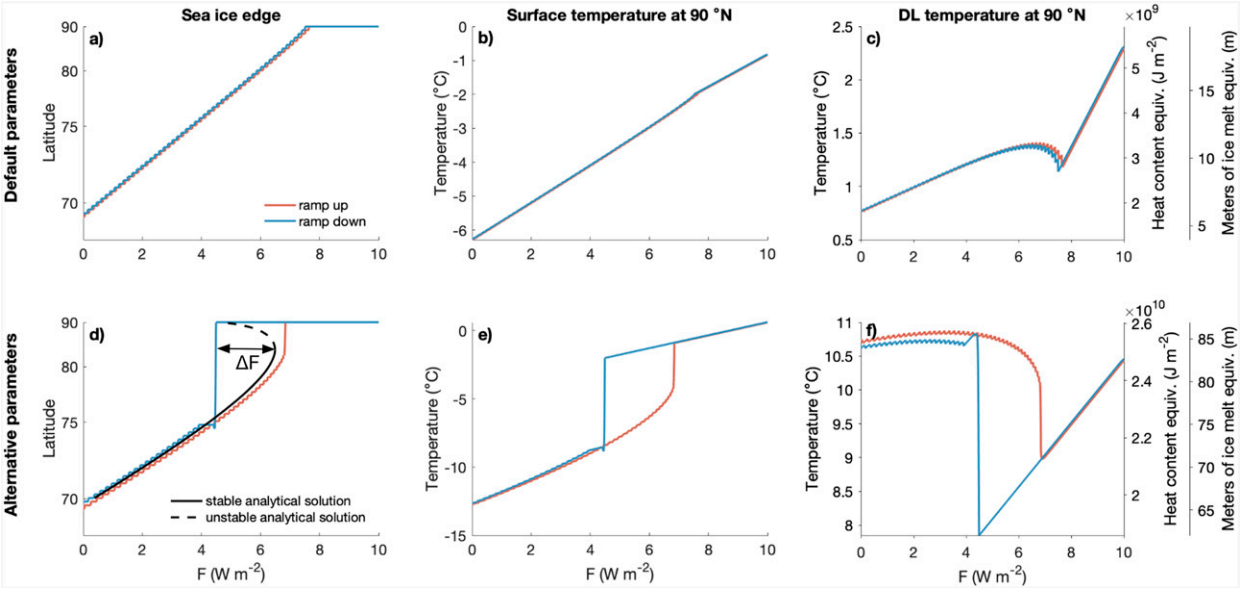

FIG. 4. Sea ice edge latitude and polar temperature in the two layers when the forcing is slowly ramped up and then ramped down. (a) The sea ice edge latitude, defined as the location at which $T_s = T_f$, when F is increased from 0 to 10 W m^{-2} (ramp up, shown in red) and when F is decreased from 10 to 0 W m^{-2} (ramp down, shown in blue). (b),(c) As in (a), but for T_s and T_d at 90°N, respectively. (top) The results under the default parameter regime and (bottom) the results under an alternative parameter regime where hysteresis occurs (values listed in parentheses Table 1). The vertical axis in (a) and (d) is scaled to be linear in sea ice area. The solid and dashed black lines in (d) show the stable and unstable states in the steady-state solution for the model.

schematically in Fig. 1, by slowly ramping the climate forcing term F up and then back down. We let the model spin up under constant forcing for 1000 years at the start of the simulation, and the forcing is then increased steadily from 0 to 10 W m^{-2} over 15 000 years. The same process is used when the forcing is ramped down from 10 to 0 W m^{-2}.

Using the default parameter regime (Table 1), which gives a simulated climate with $F = 0$ that is approximately consistent with observational estimates (Figs. 3a–c), we find that no hysteresis occurs (Figs. 4a–c). The sea ice edge displays an approximately linear retreat and growth when the forcing is ramped up and down. Next, we examine whether hysteresis can occur in other parameter regimes. Based on the schematic in Fig. 1, increasing the horizontal heat transport coefficient in the deep layer should make hysteresis more likely because it allows more heat supply to the deep polar ocean, and decreasing the horizontal heat transport coefficient in the surface layer should make hysteresis more likely because it reduces the influence of the subpolar surface ocean on the polar surface ocean. Hence we examine the simulated climate in an alternative parameter regime that has an increased value of D_d and a decreased value of D_s. In this alternative parameter regime we also reduce the vertical heat flux coefficient when ice is present in order to enhance the jump in heat flux when the climate is varied. The alternative parameter values are listed in parentheses in Table 1.

We find that a striking hysteresis occurs in this alternative parameter regime (Figs. 4d–f). The steady-state solution (black solid and dashed lines in Fig. 4d) indicates that there is an unstable climate state for climate forcing values between around $F = 4.5$ and 6.5 W m^{-2}. The bifurcation points at the edge of this range coincide with the edges of the hysteresis loop in the numerical solution. The spatial structures of the temperature and horizontal heat transport in each model layer, as well as the vertical heat flux between the layers, are shown in Fig. 5 for the cold and warm states under the same climate forcing. The state with a warmer surface temperature in high latitudes clearly has a colder deep layer temperature in high latitudes, as anticipated in the conceptual sketch (Fig. 1). And although it is difficult to discern in Fig. 5, the state with a warmer high-latitude surface temperature has a slightly colder surface temperature in lower latitudes (note that this small temperature difference is not indicated in the schematic in Fig. 1). This is because the bistability involves only heat transport feedbacks and not radiative feedbacks. Thus, the global-mean outgoing longwave radiation needs to be the same in both states, which in this idealized model implies the same global-mean surface temperature. This feature of the two states is in contrast to bistability brought on by the ice–albedo feedback or other radiative feedbacks.

Note that in the default parameter regime, atmospheric and oceanic heat transport have a meridional maximum of 3.2 and 0.8 PW, respectively, which is approximately in line with the partitioning of heat transport from observational estimates and other EBM-style models (e.g., Armour et al. 2019). However, the partitioning of heat transport is different in the alternative parameter regime where hysteresis occurs (Figs. 5c,f).

Next, we consider many values for the horizontal heat transport coefficients in the surface and deep layers. For each set of coefficients, we compute the width of the hysteresis loop (ΔF indicated in Fig. 4d) using the steady-state solution of the model. Here, ΔF is computed as the maximum forcing

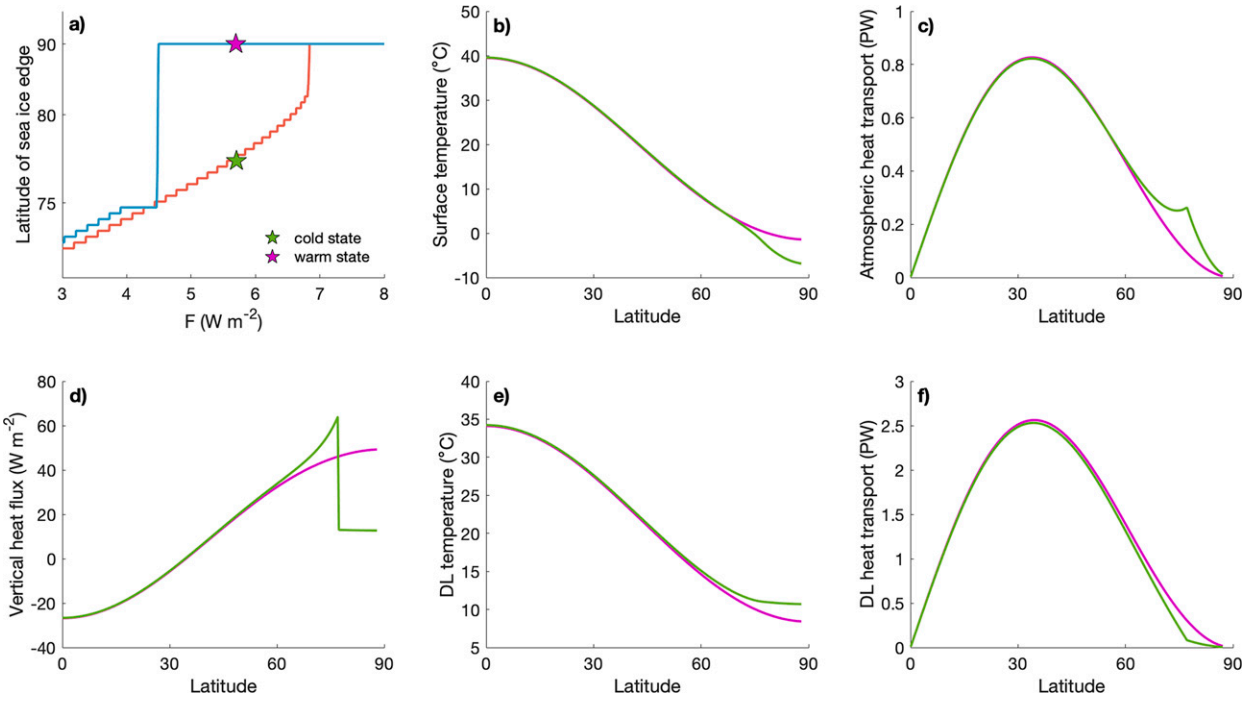

FIG. 5. Temperature and heat transport for the two stable climate states. (a) Sea ice edge (latitude where $T_s = T_f$) in the model under the alternative parameter regime when the forcing F is slowly ramped up and ramped down, as in Fig. 4d but using a narrower range of forcing values. The two stars indicate two stable climate states under the same forcing $F = 5.7$ W m^{-2}: a cold state (green star) and a warm state (pink star). (b) Surface temperature (T_s), (c) atmospheric meridional heat transport, (d) vertical heat flux between the two layers, (e) DL temperature (T_d), and (f) DL meridional heat transport; the spatial structure of each of these fields is plotted for the cold state (green curves) and warm state (pink curves) with $F = 5.7$ W m^{-2}.

at which the model can have ice (first saddle-node bifurcation) minus the minimum forcing at which the model can be ice-free (second saddle-node bifurcation); $\Delta F = 0$ in simulations with no hysteresis. The results are shown in Fig. 6.

The occurrence of a bifurcation in some parameter regimes is meaningful because it signifies that in those regimes there is a range of forcing values for which there exist two stable climate states with different sea ice edges under the same greenhouse forcing. During forced warming or cooling, an abrupt jump between the two states occurs when the bifurcation point (or tipping point) is crossed.

b. *Storage and release of heat*

The simulated DL has a more horizontally uniform temperature distribution than the SML, with the DL being colder than the SML in low latitudes and warmer than the SML in high latitudes (Fig. 3). As can be inferred from Eq. (4), the global-mean temperature of the DL would be equal to the SML if k were globally uniform, but variations in k cause an offset between the temperatures of the two layers.

The temperature of the DL tends to rise with increasing climate forcing F. However, at high-latitude locations where the surface becomes ice free ($T_s > T_f$), the mixing coefficient increases so that more heat is transported out of the DL and into the colder SML above. This causes the DL temperature in high latitudes to drop as the model approaches an ice-free state. In the alternative parameter regime which has hysteresis, there is a sudden drop in the DL temperature when warming causes the model to cross the bifurcation point, with an associated release of heat equivalent to about 15 m of ice melt (Fig. 4f). In the default parameter regime which has no hysteresis, there is no sudden drop in the DL temperature, but there is still a gradual decrease in DL temperature, with a release of heat equivalent to about 2 m of ice melt (Fig. 4c). This implies that even in the absence of hysteresis, the change in the vertical mixing coefficient can lead to enough heat being released from the DL to dramatically melt the sea ice.

In both cases, this is only a small fraction of the total heat stored in the DL, which has the potential to melt 10–85 m of ice depending on the model parameters. We find this to be true for a range of parameter values that produce hysteresis. To demonstrate this, we measure the fraction of heat lost in the DL, $H = (T_d^{\max} - T_d^{\min})/T_d^{\max}$, where $T_d^{\max}$ is the DL temperature maximum before the bifurcation and $T_d^{\min}$ is the DL temperature minimum after the bifurcation. We then compare the heat loss percentage (H) to the amount of hysteresis (ΔF), and we vary the horizontal and vertical heat transport coefficients, starting from a parameter regime which allows hysteresis. A larger value of D_d or a smaller value of D_s both lead to more hysteresis, as does a larger vertical heat transport coefficient in ice-free conditions (Figs. 7d–f). However, there is no consistent relationship between the amount of hysteresis and the percentage of stored heat released. The percentage of stored

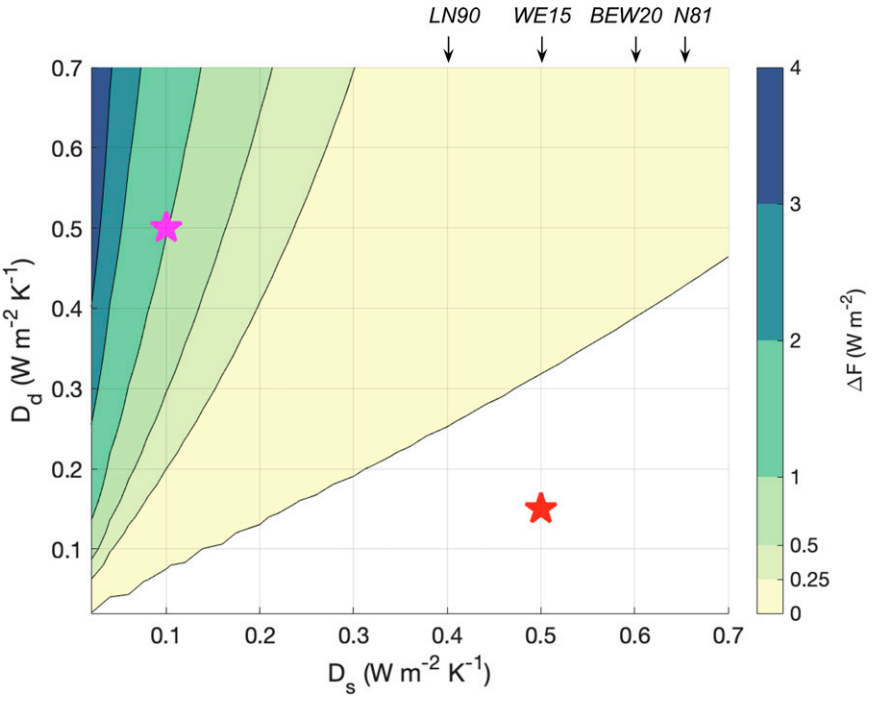

FIG. 6. Level of hysteresis when the horizontal heat transport coefficients D_s and D_d are varied. Other parameters are set to their default values (Table 1). Here hysteresis is measured as the range of forcing values with bistability ΔF, using the steady-state solution as indicated in Fig. 4d. The values of D_s and D_d used in the default parameter regime and the alternative parameter regime are indicated by the red and magenta stars, respectively. Note that the level of hysteresis indicated by the magenta star is different from the level of hysteresis in Fig. 4d due to different $k_{\text{ice-covered}}$ values. Values for D_s used in previous studies with idealized models that had a similar surface layer are indicted by arrows along the top of the figure [LN90 is Lin and North (1990), WE15 is Wagner and Eisenman (2015), BEW20 is Beer et al. (2020), and N81 is North et al. (1981)].

heat that is released increases for larger values of $k_{\text{ice-free}}$, decreases for larger values D_d, and remains largely unaffected by variations D_s (Fig. 7a). Nonetheless, the small fraction of heat that is lost from the DL when the system crosses the bifurcation point in a ramp-up simulation is striking.

How relative heat loss varies with these parameters can be understood by considering the DL heat maximum before the bifurcation point and the amount of heat loss (Figs. 7b,c). A larger value of $k_{\text{ice-free}}$ leads to a smaller heat maximum in the DL due to increased vertical heat transport. It also leads to a larger heat loss, and therefore a larger heat loss percentage. A larger value of D_d leads to a larger heat maximum in the DL but minimal change in the amount of heat lost, and therefore a smaller heat loss percentage. A smaller value of D_s sustains a larger temperature difference between the two layers at the pole, which leads to a larger heat maximum in the DL and a larger heat loss, so its heat loss percentage remains largely unchanged.

c. Caveats

The current study describes a highly idealized model, which is intended to isolate a single process. There are caveats in interpreting results from this idealized system in the context of a world with numerous interacting processes. For example, the model only represents annual-mean temperature. In the case of the surface albedo feedback, including a seasonal cycle diminishes the degree of hysteresis (Wagner and Eisenman 2015). However, the role of the seasonal cycle is less straightforward in the case of vertical mixing, for which winter storms have a large effect. Furthermore, we only consider steady-state climates in our analysis. The change in heat storage does not directly correspond with sea ice volume loss in steady-state climates, in contrast with transient climate changes. For example, when changing only the depth of the DL in the steady-state analysis, the amount of heat storage is altered, as is the heat loss when transitioning to an ice-free state. However, the heat loss percentage remains unchanged, as does the amount of hysteresis and the change in the DL temperature, which we focus on in the present analysis.

Given the simple representations of heat transport in the atmosphere and ocean, the values of the heat transport coefficients are not well constrained. Previous studies have used a similar representation for primarily atmospheric heat transport, and we use these to guide the value of D_s. However, since the two-layer model presented in this paper includes heat transport in the lower layer, it would be reasonable to

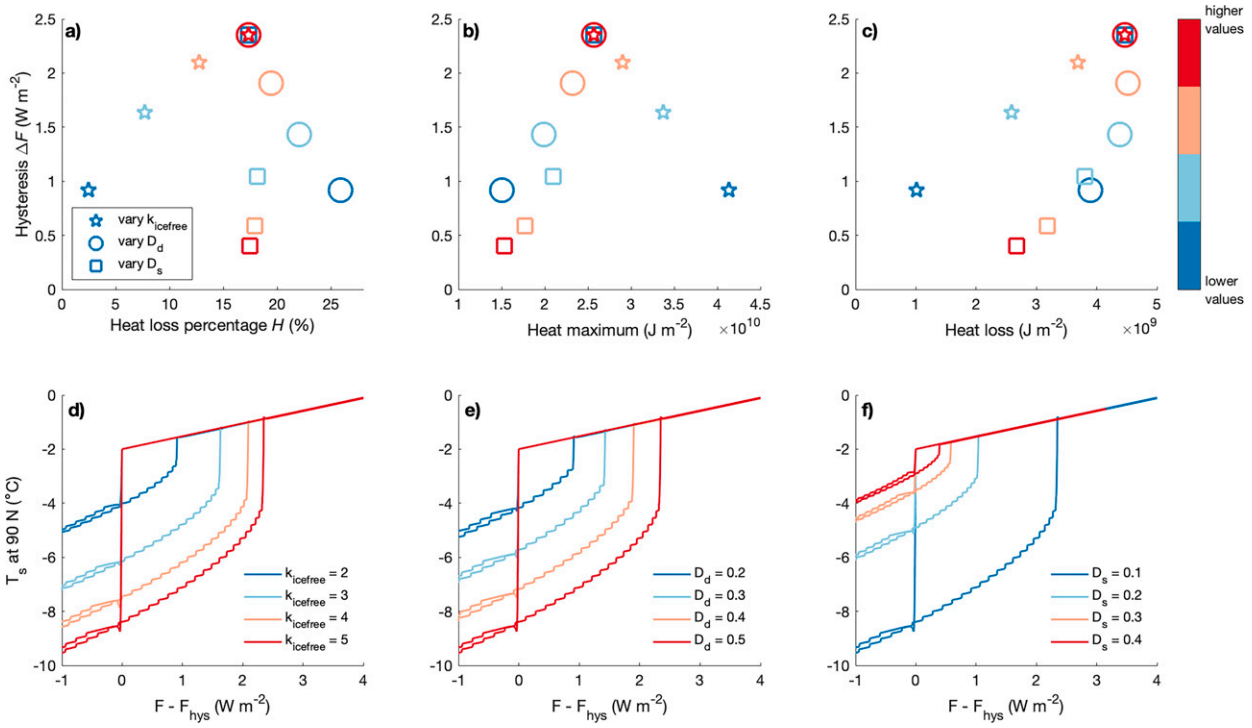

FIG. 7. (top) Hysteresis width ΔF vs (a) the percentage of heat lost H from the DL, (b) the heat maximum before the bifurcation in the DL, and (c) the heat loss from the DL during the bifurcation for simulations in a number of different parameter regimes. Star symbols indicate simulations where $k_{\text{ice-free}}$ is varied and all other parameters are set to the values indicated in parenthesis in Table 1. Circles and squares indicate simulations with varied D_d and D_s. The specific values of $k_{\text{ice-free}}$, D_d, D_s are specified in (d)–(f) and are identified with the same color in (a)–(c). (bottom) The surface temperature at 90°N when forcing is ramped up and ramped down in the alternative parameter regime ($k_{\text{ice-free}} = 5$, $D_d = 0.5$, $D_s = 0.1$) and using three other values of (d) $k_{\text{ice-free}}$, (e) D_d, and (f) D_s (values indicated in W m^{-2} K^{-1}). The horizontal axis shows the forcing anomaly relative to the value of F at which the first bifurcation occurs, F_{hys}.

use a lower value of D_s compared with previous one-layer models. The value of D_d is tuned so that the model output approximately matches observations. However, the DL temperature does not match well in low latitudes. It is therefore plausible that a larger value of D_d would be more appropriate. This could have implications for a possible hysteresis, and we explore the impacts of variations in the values of D_s and D_d for two further parameter cases in Figs. 3d–f (as discussed above). For one of the two variations ($D_s = 0.4$, $D_d = 0.3$), hysteresis occurs.

5. Summary and discussion

In this study, we use an idealized model of the global climate to investigate the possible impacts of a proposed wind–ice–ocean feedback between retreating sea ice and enhanced ocean mixing. This has consequences for the release of heat stored in the deep Arctic Ocean, causing the sea ice retreat to accelerate. We find this feedback can cause a novel bistability in the climate system, with an associated hysteresis occurring under forced warming and cooling. The hysteresis loop is characterized by an abrupt and irreversible transition to ice-free conditions when the bifurcation point is crossed during gradual forced warming.

However, we find that hysteresis occurs in only a limited range of the model parameter space. For the parameter regime that gives rise to temperatures that most closely resemble the current climate, hysteresis does not occur. This could imply that bistable regimes only occur for climates with unrealistic deep water temperatures and heat transports, but note that given the idealized nature of the model, the parameter regime that gives rise to the most realistic temperature distribution may not give rise to the most realistic response to forced heating. Hence we conclude that hysteresis is possible in principle due to this feedback, but we are not able to determine whether this hysteresis can occur in the real world. The reversibility of Arctic sea ice loss has been investigated in comprehensive climate models, and no evidence of hysteresis has been found (Armour et al. 2011; Li et al. 2013). However, the wind–ice–ocean feedback may not be well represented in these models (even if it is present in the physical ocean) due to the limits of coarse-resolution mixing parameterizations and poorly resolved upper-ocean processes in the Arctic Ocean. For example, Manucharyan and Thompson (2022) suggest that such coarse-resolution climate models may not capture the changes in the dissipation of eddies under sea ice retreat. In a higher-resolution model, they found that sea ice loss reduced the dissipation of upper-ocean eddies, allowing more subsurface heat to be brought into the mixed layer and creating a positive feedback. Thus, high-resolution models could be used to further explore this feedback.

A consequence of hysteresis is the abrupt release of heat from the subsurface layer, which has enough heat to melt tens of meters of sea ice. However, even without hysteresis, the wind–ice–ocean feedback enhances vertical mixing in the Arctic Ocean, which leads to a decrease in the subsurface temperature. In the parameter regime that gives rise to temperatures that most closely resemble the current climate, this reduction of heat is equivalent to about 2 m of ice melt.

We find that even though there is enough heat in the deep Arctic Ocean to melt all the Arctic sea ice many times over, only a small fraction of the stored heat is released during warming, whether or not hysteresis occurs. This suggests the current amount of heat stored in the Atlantic Water layer in the deep Arctic Ocean is not a good indicator of how much subsurface heat will reach the surface as the Arctic sea ice retreats. We furthermore show that the percentage of heat lost from the deep Arctic Ocean is not robustly related to the amount of hysteresis in the model.

By caveat, there are many aspects of the climate that could influence this feedback but are not included in the present idealized model. For example, it is possible that increased river runoff or net precipitation changes in a warming climate could lead to an increase in salinity stratification in the Arctic Ocean, which would further isolate heat in the DL and could mask the effects of this feedback (as reviewed in Timmermans and Marshall 2020). On the other hand, we also omit the surface albedo feedback, which could plausibly work together with the proposed positive feedback to accelerate sea ice decline. Therefore, work using more complex models and observations is called for to further investigate how this feedback interacts with the rest of the climate system.

Acknowledgments. Thanks to Tim Merlis, Nicole Shibley, Marion Alberty, and Jen MacKinnon for helpful discussions and also to two anonymous reviewers for helpful comments. This work was supported by National Science Foundation Grant OCE-2048590.

Data availability statement. The Levitus94 data used in Figs. 2b and 3 were downloaded online (from http://iridl.ldeo.columbia.edu). The model code is available on GitHub (at https://github.com/emma-beer/two-ocean-layer-EBM-2022).

APPENDIX A

Model Numerics

We numerically integrate the system in Eqs. (1)–(5) using implicit Euler time stepping and centered differencing in space.

a. Implicit Euler time stepping

Using implicit Euler time stepping (with time index n), Eqs. (1)–(4) can be written as

$$\mathbf{k}^n = \begin{cases} k_{\text{ice-free}} & \mathbf{T}_s^n > T_f \\ k_{\text{ice-covered}} & \mathbf{T}_s^n \le T_f \end{cases}, \tag{A1}$$

$$\mathbf{T}_s^{n+1} - \mathbf{T}_s^n = \frac{\Delta t}{c_s}[\mathbf{C} - \mathbf{M}_s^n(\mathbf{T}_s^{n+1} - T_f) + \mathbf{N}_s^n(\mathbf{T}_d^{n+1} - T_f)], \tag{A2}$$

$$\mathbf{T}_d^{n+1} - \mathbf{T}_d^n = \frac{\Delta t}{c_d}[-\mathbf{M}_d^n(\mathbf{T}_d^{n+1} - T_f) + \mathbf{N}_d^n(\mathbf{T}_s^{n+1} - T_f)]. \tag{A3}$$

In Eq. (A2), we have defined the vector $\mathbf{C} \equiv (1 - \text{diag}(\boldsymbol{\alpha}))\mathbf{S} - A + F$ and matrices $\mathbf{M}_s^n = B\mathbf{I} - D_s\boldsymbol{\Lambda} + \text{diag}(\mathbf{K}^n)$ and $\mathbf{N}_s^n = \text{diag}(\mathbf{k}^n)$, where

$$\mathbf{K}^n \equiv \begin{cases} \mathbf{k}^n & \mathbf{T}_s^n > T_f \\ 0 & \mathbf{T}_s^n \le T_f \end{cases},$$

$\mathbf{I}$ is the identity matrix, and $\boldsymbol{\Lambda} \equiv \partial_x[(1 - x^2)\partial_x]$ is the diffusion operator. The operator diag($\mathbf{v}$) constructs a diagonal matrix with the vector $\mathbf{v}$ along the main diagonal. Similarly in Eq. (A3), we have defined the matrices $\mathbf{M}_d^n \equiv -D_d\boldsymbol{\Lambda} + \text{diag}(\mathbf{k}^n)$ and $\mathbf{N}_d^n = \text{diag}(\mathbf{K}^n)$.

The temperatures at time $n + 1$ can then be calculated as

$$\mathbf{T}_s^{n+1} - T_f = \left[\mathbf{I} + \frac{\Delta t}{c_s}\mathbf{M}_s^n - \frac{\Delta t^2}{c_s c_d}\mathbf{N}_s^n\left(\mathbf{I} + \frac{\Delta t}{c_d}\mathbf{M}_d^n\right)^{-1}\mathbf{N}_d^n\right]^{-1}\left[\mathbf{T}_s^n - T_f + \frac{\Delta t}{c_s}\mathbf{C} + \frac{\Delta t}{c_s}\mathbf{N}_s^n\left(I + \frac{\Delta t}{c_d}\mathbf{M}_d^n\right)^{-1}(\mathbf{T}_d^n - T_f)\right], \tag{A4}$$

$$\mathbf{T}_d^{n+1} - T_f = \left(\mathbf{I} + \frac{\Delta t}{c_d}\mathbf{M}_d^n\right)^{-1}\left[\mathbf{T}_d^n - T_f + \frac{\Delta t}{c_d}\mathbf{N}_d^n(\mathbf{T}_s^{n+1} - T_f)\right]. \tag{A5}$$

b. Diffusion operator with central difference

We use a central difference spatial derivative stencil for the diffusion operator [Eq. (5)]. The model output and diffusion operator are defined on staggered grids. Using a first-order central difference scheme (spatial grid points indexed with i), $\partial T/\partial x$ can be written as

$$\left(\frac{\partial T}{\partial x}\right)_i = \frac{T_{i+1/2} - T_{i-1/2}}{\Delta x}. \tag{A6}$$

Next, we define $\gamma_i \equiv (1 - x_i^2)[(T_{i+1/2} - T_{i-1/2})/\Delta x]$. Using another first-order central difference scheme, $\partial\gamma/\partial x$ can be written as

$$\left(\frac{\partial \gamma}{\partial x}\right)_i = \frac{1}{\Delta x^2}\{(1 - x_{i+1/2}^2)T_{i+1} - [(1 - x_{i+1/2}^2) + (1 - x_{i-1/2}^2)]T_i + (1 - x_{1-1/2}^2)T_{i-1}\}. \tag{A7}$$

Finally, we construct a diffusion operator matrix $\boldsymbol{\Lambda}$ to act on T with:

$$\Lambda_{i,i-1} = \frac{1}{\Delta x^2}(1 - x_{i-1/2}^2), \tag{A8}$$

$$\Lambda_{i,i} = \frac{1}{\Delta x^2}[(1 - x_{i-1/2}^2) + (1 - x_{i+1/2}^2)], \tag{A9}$$

$$\Lambda_{i,i+1} = \frac{1}{\Delta x^2}(1 - x_{i+1/2}^2). \tag{A10}$$

APPENDIX B

Model Steady-State Solution Using Legendre Polynomial Expansions

We calculate an approximate steady-state solution by expressing the temperature as an expansion of Legendre polynomials. Using Legendre polynomials is not essential to obtaining a steady-state solution, which could alternatively be done by inverting the diffusion operator matrices to get a solution of the spatially gridded algebraic equations, but it reduces the computation time substantially. To do this, we rewrite the jump in the vertical heat flux coefficient as a function of the ice edge latitude x_s and use Legendre polynomial identities to write an expression for the surface temperature. Since the surface temperature is at the freezing point at the ice edge, the forcing can then be calculated as a function of the ice edge latitude. An expansion of Legendre polynomials needs to then be calculated at each individual ice edge latitude, which is somewhat different from previous EBM solutions that included a surface albedo feedback but not a second layer (North et al. 1981).

First we rewrite Eqs. (1)–(5) in equilibrium with x_s defined as the latitude where $T_s = T_f$:

$$\begin{aligned} 0 = {} & [1 - \alpha(x)]S(x) - A - B[T_s(x) - T_f] \\ & + D_s\partial_x[(1 - x^2)\partial_x T_s(x)] + k(x, x_s)[T_d(x) \\ & - T_{\mathrm{SML}}(x, x_s)] + F, \end{aligned} \tag{B1}$$

$$0 = D_d\partial_x[(1 - x^2)\partial_x T_d(x)] + k(x, x_s)[T_{\mathrm{SML}}(x, x_s) - T_d(x)], \tag{B2}$$

$$\text{with} \quad k = \begin{cases} k_{\text{ice-covered}}, & x > x_s \\ k_{\text{ice-free}}, & x \le x_s \end{cases} \text{ and } T_{\mathrm{SML}} = \begin{cases} T_f, & x > x_s \\ T_s(x), & x \le x_s \end{cases}. \tag{B3}$$

Next we introduce solutions to T_s and T_d as a sum of Legendre polynomials P_n:

$$T_s(x) - T_f = \sum_{n_{\text{even}}} T_n P_n(x), \quad T_d(x) - T_f = \sum_{n_{\text{even}}} V_n P_n(x). \tag{B4}$$

Next we multiply Eqs. (B1) and (B2) by $(2m + 1)P_m(x)$ and integrate between 0 and 1, using the definitions in Eq. (B4) and orthogonality relation to simplify:

$$\begin{aligned} 0 = {} & \delta_{0,m}(F - A) + L_m - BT_m - m(m + 1)D_s T_m \\ & + (2m + 1)\sum_{n_{\text{even}}} V_n \int_0^1 k(x, x_s)P_n(x)P_m(x)dx \\ & - (2m + 1)\sum_{n_{\text{even}}} T_n \int_0^{x_s} k(x, x_s)P_n(x)P_m(x)dx, \end{aligned} \tag{B5}$$

$$\begin{aligned} 0 = {} & -m(m + 1)D_d V_m \\ & + (2m + 1)\sum_{n_{\text{even}}} T_n \int_0^{x_s} k(x, x_s)P_n(x)P_m(x)dx \\ & - (2m + 1)\sum_{n_{\text{even}}} V_n \int_0^1 k(x, x_s)P_n(x)P_m(x)dx, \end{aligned} \tag{B6}$$

$$\text{with} \quad L_m = (2m + 1)\int_0^1 [1 - \alpha(x)]S(x)P_m(x)dx. \tag{B7}$$

Next we insert the definition of k (B3) into Eqs. (B5)–(B7) and simplify:

$$\begin{aligned} 0 = {} & \delta_{0,m}(F - A) + L_m - BT_m - m(m + 1)D_s T_m + k_{\text{ice-covered}} V_m \\ & + \sum_{n_{\text{even}}} [\Delta k V_n - k_{\text{ice-free}} T_n] I_m^n(x_s), \end{aligned} \tag{B8}$$

$$\begin{aligned} 0 = {} & -m(m + 1)D_d V_m - k_{\text{ice-covered}} V_m \\ & + \sum_{n_{\text{even}}} [k_{\text{ice-free}} T_n - \Delta k V_n] I_m^n(x_s), \end{aligned} \tag{B9}$$

$$\text{where} \quad \Delta k = k_{\text{ice-free}} - k_{\text{ice-covered}} \quad \text{and}$$

$$I_m^n(x_s) = (2m + 1)\int_0^{x_s} P_n(x)P_m(x)dx. \tag{B10}$$

We truncate at $n = 80$ and solve for $T_m(x_s, F)$, $V_m(x_s, F)$. Then the surface temperature can be written as

$$T_s(x) - T_f = \sum_{m_{\text{even}}}^{80} T_m(x_s, F)P_m(x). \tag{B11}$$

Using that $T_s = T_f$ at $x = x_s$, we are left with the expression

$$0 = \sum_{m_{\text{even}}}^{80} T_m(x_s, F)P_m(x_s). \tag{B12}$$

We can then solve for $F(x_s)$. Because the solution for T_m includes a sum over index n, an expansion of Legendre polynomials needs to be calculated at each ice edge latitude x_s, as noted above.

REFERENCES

Ardyna, M., M. Babin, M. Gosselin, E. Devred, L. Rainville, and J.-E. Tremblay, 2014: Recent Arctic Ocean sea ice loss triggers novel fall phytoplankton blooms. *Geophys. Res. Lett.*, **41**, 6207–6212, https://doi.org/10.1002/2014GL061047.

Armour, K. C., I. Eisenman, E. Blanchard-Wrigglesworth, K. E. McCusker, and C. M. Bitz, 2011: The reversibility of sea ice loss in a state-of-the-art climate model. *Geophys. Res. Lett.*, **38**, L16705, https://doi.org/10.1029/2011GL048739.

——, N. Siler, A. Donohoe, and G. H. Roe, 2019: Meridional atmospheric heat transport constrained by energetics and mediated by large-scale diffusion. *J. Climate*, **32**, 3655–3680, https://doi.org/10.1175/JCLI-D-18-0563.1.

Arthun, M., T. Eldevik, L. H. Smedsrud, O. Skagseth, and R. B. Ingvaldsen, 2012: Quantifying the influence of Atlantic heat on Barents Sea ice variability and retreat. *J. Climate*, **25**, 4736–4743, https://doi.org/10.1175/JCLI-D-11-00466.1.

Beer, E., I. Eisenman, and T. J. W. Wagner, 2020: Polar amplification due to enhanced heat flux across the halocline. *Geophys. Res. Lett.*, **47**, e2019GL086706, https://doi.org/10.1029/2019GL086706.

Budyko, M., 1969: Effect of solar radiation variations on climate of Earth. *Tellus*, **21A**, 611, https://doi.org/10.3402/tellusa.v21i5.10109.

Carmack, E., and Coauthors, 2015: Toward quantifying the increasing role of oceanic heat in sea ice loss in the new Arctic. *Bull. Amer. Meteor. Soc.*, **96**, 2079–2105, https://doi.org/10.1175/BAMS-D-13-00177.1.

Cole, S. T., J. M. Toole, L. Rainville, and C. M. Lee, 2018: Internal waves in the Arctic: Influence of ice concentration, ice roughness, and surface layer stratification. *J. Geophys. Res. Oceans*, **123**, 5571–5586, https://doi.org/10.1029/2018JC014096.

Cummins, P. F., D. Masson, and O. A. Saenko, 2016: Vertical heat flux in the ocean: Estimates from observations and from a coupled general circulation model. *J. Geophys. Res. Oceans*, **121**, 3790–3802, https://doi.org/10.1002/2016JC011647.

D'Asaro, E., and J. Morison, 1992: Internal waves and mixing in the Arctic-Ocean. *Deep-Sea Res.*, **39A**, S459–S484, https://doi.org/10.1016/S0198-0149(06)80016-6.

Davis, P. E. D., C. Lique, H. L. Johnson, and J. D. Guthrie, 2016: Competing effects of elevated vertical mixing and increased freshwater input on the stratification and sea ice cover in a changing Arctic Ocean. *J. Phys. Oceanogr.*, **46**, 1531–1553, https://doi.org/10.1175/JPO-D-15-0174.1.

Dosser, H. V., and L. Rainville, 2016: Dynamics of the changing near-inertial internal wave field in the Arctic Ocean. *J. Phys. Oceanogr.*, **46**, 395–415, https://doi.org/10.1175/JPO-D-15-0056.1.

——, M. Chanona, S. Waterman, N. C. Shibley, and M. L. Timmermans, 2021: Changes in internal wave-driven mixing across the Arctic Ocean: Finescale estimates from an 18-year pan-arctic record. *Geophys. Res. Lett.*, **48**, e2020GL091747, https://doi.org/10.1029/2020GL091747.

Eisenman, I., and J. S. Wettlaufer, 2009: Nonlinear threshold behavior during the loss of Arctic sea ice. *Proc. Natl. Acad. Sci. USA*, **106**, 28–32, https://doi.org/10.1073/pnas.0806887106.

Fer, I., 2009: Weak vertical diffusion allows maintenance of cold halocline in the central Arctic. *Atmos. Ocean. Sci. Lett.*, **2**, 148–152, https://doi.org/10.1080/16742834.2009.11446789.

Fine, E. C., and S. T. Cole, 2022: Decadal observations of internal wave energy, shear, and mixing in the western Arctic Ocean. *J. Geophys. Res. Oceans*, **127**, e2021JC018056, https://doi.org/10.1029/2021JC018056.

——, M. H. Alford, J. A. MacKinnon, and J. B. Mickett, 2021: Microstructure mixing observations and finescale parameterizations in the Beaufort Sea. *J. Phys. Oceanogr.*, **51**, 19–35, https://doi.org/10.1175/JPO-D-19-0233.1.

Gregory, J., 2000: Vertical heat transports in the ocean and their effect an time-dependent climate change. *Climate Dyn.*, **16**, 501–515, https://doi.org/10.1007/s003820000059.

Held, I. M., M. Winton, K. Takahashi, T. Delworth, F. Zeng, and G. K. Vallis, 2010: Probing the fast and slow components of global warming by returning abruptly to preindustrial forcing. *J. Climate*, **23**, 2418–2427, https://doi.org/10.1175/2009JCLI3466.1.

Levitus, S., and T. Boyer, 1994: *Temperature*. Vol. 4, *World Ocean Atlas 1994*, NOAA Atlas NESDIS 4, 117 pp.

——, R. Burgett, and T. P. Boyer, 1994: *Salinity*. Vol. 3, *World Ocean Atlas 1994*, NOAA Atlas NESDIS 3, 99 pp.

Li, C., D. Notz, S. Tietsche, and J. Marotzke, 2013: The transient versus the equilibrium response of sea ice to global warming. *J. Climate*, **26**, 5624–5636, https://doi.org/10.1175/JCLI-D-12-00492.1.

Lin, R., and G. North, 1990: A study of abrupt climate change in a simple nonlinear climate model. *Climate Dyn.*, **4**, 253–261, https://doi.org/10.1007/BF00211062.

Lincoln, B. J., T. P. Rippeth, Y.-D. Lenn, M. L. Timmermans, W. J. Williams, and S. Bacon, 2016: Wind-driven mixing at intermediate depths in an ice-free Arctic Ocean. *Geophys. Res. Lett.*, **43**, 9749–9756, https://doi.org/10.1002/2016GL070454.

Liu, Q., A. V. Babanin, S. Zieger, I. R. Young, and C. Guan, 2016: Wind and wave climate in the Arctic Ocean as observed by altimeters. *J. Climate*, **29**, 7957–7975, https://doi.org/10.1175/JCLI-D-16-0219.1.

Manucharyan, G. E., and A. F. Thompson, 2022: Heavy footprints of upper-ocean eddies on weakened Arctic sea ice in marginal ice zones. *Nat. Commun.*, **13**, 2147, https://doi.org/10.1038/s41467-022-29663-0.

Morison, J., C. Long, and M. Levine, 1985: Internal wave dissipation under sea ice. *J. Geophys. Res.*, **90**, 1959–1966, https://doi.org/10.1029/JC090iC06p11959.

Nishino, S., Y. Kawaguchi, J. Inoue, T. Hirawake, A. Fujiwara, R. Futsuki, J. Onodera, and M. Aoyama, 2015: Nutrient supply and biological response to wind-induced mixing, inertial motion, internal waves, and currents in the northern Chukchi Sea. *J. Geophys. Res. Oceans*, **120**, 1975–1992, https://doi.org/10.1002/2014JC010407.

North, G., 1975: Theory of energy-balance climate models. *J. Atmos. Sci.*, **32**, 2033–2043, https://doi.org/10.1175/1520-0469(1975)032<2033:TOEBCM>2.0.CO;2.

——, R. Cahalan, and J. Coakley, 1981: Energy-balance climate models. *Rev. Geophys.*, **19**, 91–121, https://doi.org/10.1029/RG019i001p00091.

Peterson, A. K., I. Fer, M. G. McPhee, and A. Randelhoff, 2017: Turbulent heat and momentum fluxes in the upper ocean under Arctic sea ice. *J. Geophys. Res. Oceans*, **122**, 1439–1456, https://doi.org/10.1002/2016JC012283.

Polyakov, I. V., and Coauthors, 2017: Greater role for Atlantic inflows on sea-ice loss in the Eurasian Basin of the Arctic Ocean. *Science*, **356**, 285–291, https://doi.org/10.1126/science.aai8204.

——, and Coauthors, 2020: Weakening of cold halocline layer exposes sea ice to oceanic heat in the eastern Arctic Ocean. *J. Climate*, **33**, 8107–8123, https://doi.org/10.1175/JCLI-D-19-0976.1.

Rainville, L., and R. A. Woodgate, 2009: Observations of internal wave generation in the seasonally ice-free Arctic. *Geophys. Res. Lett.*, **36**, L23604, https://doi.org/10.1029/2009GL041291.

Reigstad, M., P. Wassmann, C. Riser, S. Oygarden, and F. Rey, 2002: Variations in hydrography, nutrients and chlorophyll a in the marginal ice-zone and the central Barents Sea. *J. Mar. Syst.*, **38**, 9–29, https://doi.org/10.1016/S0924-7963(02)00167-7.

Rippeth, T. P., B. J. Lincoln, Y.-D. Lenn, J. A. M. Green, A. Sundfjord, and S. Bacon, 2015: Tide-mediated warming of Arctic halocline by Atlantic heat fluxes over rough topography. *Nat. Geosci.*, **8**, 191–194, https://doi.org/10.1038/ngeo2350.

Sellers, W. D., 1969: A global climatic model based on the energy balance of the Earth–atmosphere system. *J. Appl. Meteor.*, **8**, 392–400, https://doi.org/10.1175/1520-0450(1969)008<0392:AGCMBO>2.0.CO;2.

Thorndike, A., 1992: A toy model linking atmospheric thermal-radiation and sea ice growth. *J. Geophys. Res.*, **97**, 9401–9410, https://doi.org/10.1029/92JC00695.

Timmermans, M.-L., and J. Marshall, 2020: Understanding Arctic Ocean circulation: A review of ocean dynamics in a changing climate. *J. Geophys. Res. Oceans*, **125**, e2018JC014378, https://doi.org/10.1029/2018JC014378.

Wagner, T. J. W., and I. Eisenman, 2015: How climate model complexity influences sea ice stability. *J. Climate*, **28**, 3998–4014, https://doi.org/10.1175/JCLI-D-14-00654.1.